Journal of Materials Chemistry A

PAPER

View Article Online
View Journal | View Issue

Cite this: J. Mater. Chem. A, 2016, 4, 13837

Effects of interfacial layers on the photoelectrochemical properties of tantalum nitride photoanodes for solar water splitting†

Chizhong Wang,[a] Takashi Hisatomi,[ab] Tsutomu Minegishi,[abc] Mamiko Nakabayashi,[d] Naoya Shibata,[d] Masao Katayama[ab] and Kazunari Domen*[ab]

Received 26th May 2016
Accepted 9th August 2016

DOI: 10.1039/c6ta04363a

www.rsc.org/MaterialsA

This work describes the effects of interlayers on the structural, crystalline and photoelectrochemical properties of Ta_3N_5 photoanodes. Nb_4N_5 interlayers with different thicknesses are formed between Ta_3N_5 films and Ta back substrates using a thin film transfer method. Zone-axis images and electron diffraction patterns of cross-sections of the resulting $Ta_3N_5/Nb_4N_5/Ta/Ti$ electrodes acquired by transmission electron microscopy evidence the formation of a 200 nm thick oriented Ta_3N_5 grain layer in the vicinity of the interlayer. This oriented Ta_3N_5 layer promotes electron transport throughout the Ta_3N_5 film. As a result, a Ta_3N_5 photoanode incorporating a Nb_4N_5 interlayer exhibits a higher photocurrent during the oxygen evolution reaction. These results obtained using the Ta_3N_5/interlayer/substrate configuration elucidate the key role played by the buffer layer in achieving efficient water splitting with Ta_3N_5 photoelectrodes.

Introduction

Photoelectrochemical (PEC) water splitting is a process used to store solar light energy *via* the formation of hydrogen.[1–3] Ta_3N_5, an n-type semiconductor, has been widely applied as a photoanode for the PEC oxygen evolution reaction (OER). With a bandgap of 2.1 eV, Ta_3N_5 absorbs visible light up to 600 nm (ref. 4) and can potentially yield a maximum photocurrent of 12.5 mA cm^{-2} under irradiation by sunlight (AM 1.5G).

Photoanodes are typically prepared as either thin films,[5] nanostructures (such as nanorods and nanotubes)[6–8] or particulate layers.[9,10] In addition, doping, surface modification and other strategies have been applied to achieve high photocurrents and negative onset potentials during PEC water oxidation.[11–16] Theoretical studies have indicated that Ta_3N_5 is an anisotropic semiconductor material in which holes are heavier than electrons,[17] resulting in low mobility of the minority charge carriers (*i.e.*, the holes), while the porosity of the Ta_3N_5 layer in a Ta_3N_5 photoanode is believed to limit the bulk transport of the majority charge carriers (electrons).[18] Controlling both the structure and crystallinity of Ta_3N_5 films is a critical aspect of improving the PEC performance of this material because these parameters significantly affect the charge separation efficiency as well as the light absorption of the Ta_3N_5.[17–20]

Studies on the growth of GaN films suggest that a GaN or AlN buffer layer will generate high crystalline quality in the upper GaN film,[21,22] and a similar effect is anticipated in the case of Ta_3N_5 film growth. In order to fabricate semiconductor/conductor configurations for use as photoelectrodes, Ta_3N_5 films are generally grown on conductive substrates, such as metallic Ta foils or Pt,[23] by nitridation under a flow of NH_3 gas and at high temperatures (800–1000 °C). To date, Ta_3N_5 photoanodes with state-of-the-art PEC performance have been fabricated on Ta foil substrates.[11,24] However, an impurity interlayer consisting of TaN_x phases is inevitably formed between the Ta_3N_5 film (or nanorods and nanotubes) and the underlying Ta foil during the nitridation process.[6,20] The effects of this interlayer on electron transport in the Ta_3N_5 film and at the Ta_3N_5/TaN_x interface are expected to alter the PEC performance of Ta_3N_5 photoanodes.

In the present work, the effects of interlayers on the growth of Ta_3N_5 films and on the PEC performance of Ta_3N_5 photoanodes were assessed by introducing a niobium nitride (NbN_x) layer at the interface between the Ta_3N_5 film and the conductive substrate by a thin film transfer technique.[25] Inert Si wafers were used as synthesis platforms for the formation of the NbN_x and Ta_3N_5 bilayer films. After the film transfer process, the NbN_x surface layer acted as a back contact to conduct photogenerated electrons

[a]Department of Chemical System Engineering, School of Engineering, The University of Tokyo, 7-3-1 Hongo, Bunkyo-ku, 113-8656 Tokyo, Japan. E-mail: domen@chemsys.t.u-tokyo.ac.jp; Fax: +81 3 5841 8838; Tel: +81 3 5841 1148

[b]Japan Technological Research Association of Artificial Photosynthetic Chemical Process (ARPChem), 2-11-9 Iwamotocho, Chiyoda-ku, 101-0032 Tokyo, Japan

[c]Japan Science and Technology Agency/Precursory Research for Embryonic Science and Technology (JST/PRESTO), Kawaguchi Center Building, 4-1-8, Honcho, Kawaguchi-shi, 332-0012 Saitama, Japan

[d]Institute of Engineering Innovation, The University of Tokyo, 2-11-16 Yayoi, Bunkyo-ku, 113-8656 Tokyo, Japan

† Electronic supplementary information (ESI) available. See DOI: 10.1039/c6ta04363a

from the Ta_3N_5 film to the back conductive layer, and the introduction of a NbN_x interlayer was found to enhance the photocurrent of the Ta_3N_5 photoanodes. The growth mechanism of the Ta_3N_5 films in the presence of the NbN_x layer and the effects of the interlayer on the structural, crystalline and PEC properties of the Ta_3N_5 films are discussed based on the results of this study.

Experimental section

Sample preparation

A NbN_x layer was introduced as an interlayer between Ta_3N_5 and a conductive substrate using a film transfer process, as depicted in Fig. 1. The sections of a single-crystal Si (100) substrate (1 × 1 cm, Nilaco) were cleaned by sequential ultrasonic irradiation over 10 min each in acetone, isopropanol and Milli-Q water (18.2 mΩ cm). Ta and Nb films with the desired thicknesses were sequentially deposited on the Si substrates by radio frequency (RF) magnetron sputtering (ULVAC, MNS-2000-RFG3) and the resulting multi-layered films were oxidized in a muffle furnace at 700 °C for 2 h with a temperature ramp rate of 15 °C min^{-1}. The Nb_2O_5/Ta_2O_5/Si samples fabricated in this manner were subsequently moved to a tube furnace and nitrided in a flow of NH_3 gas (100 sccm) at 900 °C for 2 h with a temperature ramp rate of 20 °C min^{-1}, forming a nitride bilayer on the Si substrates. To transfer these nitride films onto a conductive substrate, metallic Ta (150 nm) and Ti (approximately 5 μm) layers were sequentially deposited on the NbN_x/Ta_3N_5/Si sample by RF magnetron sputtering, serving as the contact and conductive layers, respectively. Because the physical contact between the Ta_3N_5 film and the Si substrate was weakened by the strain imparted upon adding the metallic Ta/Ti layers, the $Ti/Ta/NbN_x/Ta_3N_5$ films were readily peeled away from the underlying Si substrate using carbon tape supported with glass plates. For comparison purposes, a Ta_3N_5/Ta/Ti film without a NbN_x interlayer was synthesized in the same manner. The electrode areas exposed to the electrolyte solution were approximately 0.2 cm^2. Each of the Ta_3N_5 films used in this work was 630 nm thick, while the thickness of the NbN_x layer varied from 50 to 200 nm.

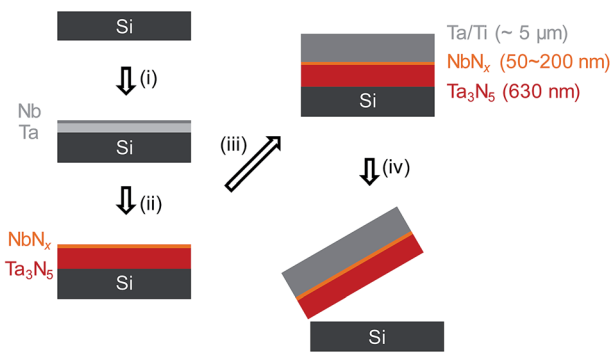

Fig. 1 Schematic diagram of the procedure used to synthesize a Ta_3N_5 film with a NbN_x interlayer. (i) Sputtering of Ta and Nb metallic films, (ii) oxidation and nitridation of the Ta/Nb films, (iii) sputtering of Ta/Ti metallic layers, and (iv) exfoliation of the NbN_x/Ta_3N_5 films from the Si substrate.

Characterization

Scanning electron microscopy (SEM, S-4700, Hitachi), transmission electron microscopy and scanning transmission electron microscopy (TEM, STEM, JEM-2800, JEOL) with energy dispersive X-ray fluorescence spectroscopy (EDX, EX-24055JGT, JEOL) were used to characterize the morphologies and structures of the thin films. Samples for cross-sectional SEM and STEM assessments were prepared by ion milling and focused ion beam (FIB) milling, respectively. X-ray diffraction (XRD) patterns were recorded using an X-ray diffractometer (Rigaku Ultima III) with Cu Kα radiation ($\lambda = 0.15405$ nm, 40 mV and 40 mA). The average crystallite size in the Ta_3N_5 films ($n = 3, \pm\sigma$) was calculated using the Scherrer equation. X-ray fluorescence spectroscopy (XPS, JEOL, JPS-90SX) was performed using Mg Kα radiation (8 kV and 10 mA), employing the C 1s peak at 284.8 eV as an internal standard to calibrate the binding energies.

Electrochemical measurement

Prior to the PEC measurements, each Ta_3N_5 photoelectrode was deposited with a thin layer of $Co(OH)_x$ using an impregnation method. This was accomplished by adding an aqueous NaOH solution (50 mM, 2.5 mL) to an aqueous $Co(NO_3)_2$ solution (6.3 mM, 10 mL) and immersing the Ta_3N_5 electrodes in the mixture for 1 h. The PEC properties of the Ta_3N_5 photoanodes were measured using a three-electrode cell with a Ag/AgCl reference electrode (in saturated aqueous KCl) and Pt wire as the counter electrode. The Ag/AgCl reference potential was converted to the reversible hydrogen electrode (RHE) potential according to the Nernst relationship

$$E\ (\text{V } \textit{vs.}\ \text{RHE}) = E\ (\text{V } \textit{vs.}\ \text{Ag/AgCl}) + 0.059 \times \text{pH} + 0.197, \quad (1)$$

where 0.197 represents the standard potential of the KCl-saturated Ag/AgCl electrode at 25 °C. An aqueous solution of potassium phosphate (KPi, 0.5 M, pH 13) was used as the electrolyte. During these trials, the Ta_3N_5 photoelectrodes were illuminated by using a chopped AM 1.5G solar simulator (San-EI Electric, XES-40S2-CE). Linear-sweep voltammetry (LSV) was employed, scanning from 1.5 to 0 V *vs.* RHE to evaluate the photocurrent density and onset potential. The photocurrent decay of each Ta_3N_5 photoelectrode was examined in the chronoamperometric mode at 1.0 V *vs.* RHE. Evolved gaseous H_2 and O_2 were simultaneously collected in an air-tight cell and quantified using a micro gas chromatograph (Agilent, 3000A, Micro GC) to calculate the faradaic efficiency.

The incident photon-to-current conversion efficiency (IPCE) was measured under monochromatic irradiation from a Xe lamp (MAX-302, Asahi Spectra) in a 0.5 M KPi electrolyte. The wavelength-dependent IPCEs were calculated using the equation

$$\text{IPCE} = 1240 \times (I_{\text{light}} - I_{\text{dark}})/(\lambda \times P_{\text{input}}) \times 100\% \quad (2)$$

where λ (nm) is the wavelength of the monochromatic irradiation, I_{light} (mA cm^{-2}) is the chronoamperometric photocurrent density, I_{dark} (mA cm^{-2}) is the dark current density and P_{input}

(mW cm^{-2}) is the incident photon density as determined by using a Si photodiode detector.

To compare the relative electrochemically active surface areas and roughness factors of different Ta_3N_5 photoelectrodes, the scan-rate dependencies of cyclic voltammograms were estimated according to a previously reported method.[26] All of the electrodes were tested at different scan rates, varying from 5 to 300 mV s^{-1}, with a capacitive current estimated at −0.1 V *vs.* Ag/AgCl. Mott–Schottky measurements were performed in a 0.5 M KPi electrolyte at a frequency of 1000 Hz with an AC amplitude of 10 mV, using an impedance analyzer (METEK, VersaSTAT3-200). The flat band potential and donor dopant density values of the Ta_3N_5 photoanodes were determined according to the Mott–Schottky relationship

$$\frac{1}{C_{SC}{}^2} = \frac{2}{\varepsilon\varepsilon_0 e N_D r^2}\left(E - E_{fb} - \frac{kT}{e}\right), \quad (3)$$

where C_{SC} (F cm^{-2}) is the space-charge capacity per surface area, ε_0 (C V^{-1} cm^{-1}) is the permittivity of free space, ε is the dielectric constant of Ta_3N_5, N_D (cm^{-3}) is the donor density, r is the roughness factor of the Ta_3N_5 electrode, k (1.38×10^{-23} J K^{-1}) is the Boltzmann constant, E (V *vs.* RHE) is the applied potential, and E_{fb} (V *vs.* RHE) represents the flat band potential of the Ta_3N_5 electrode. The flat band potential could be derived from the x-axis intercept, while the donor density could be obtained from the slope of a Mott–Schottky plot. Electrochemical impedance spectra (EIS) were measured from 100 kHz to 0.1 Hz using an impedance analyzer under simulated AM 1.5G light in a 0.5 M KPi electrolyte. To alleviate the photocorrosion of Ta_3N_5 photoelectrodes, all the samples were tested in the presence of sacrificial reagent 0.5 M $SO_3{}^{2-}$ at 1.0 V *vs.* RHE. The obtained Nyquist plots were fitted from 100 kHz to 1 Hz with an equivalent circuit model to rule out the fluctuations at frequency lower than 1 Hz.

Results and discussion

Structure and crystallinity

A top-view SEM image of a Ta_3N_5/NbN_x/Ta/Ti sample after the thin film transfer is shown in Fig. 2(a). The surface of the Ta_3N_5 film exhibits roughness originating from the porous contact at the Ta_3N_5/Si interface in the parent NbN_x/Ta_3N_5/Si sample. The possible exposure of the NbN_x interlayer to the film surface is ruled out by the XPS data obtained from the Ta_3N_5/NbN_x/Ta/Ti film, as shown in Fig. S1.† In addition, the absence of Ta species on the surface of the parent NbN_x/Ta_3N_5/Si sample suggests that the Ta_3N_5 film was not in direct contact with the underlying metallic substrate. The layered structure of the Ta_3N_5/NbN_x/Ta/Ti sample is clearly observed in the cross-sectional SEM image presented in Fig. 2(b). Here, the NbN_x layer is evident as a region of darker contrast, with a thickness of approximately 100 nm. In the magnified view, a porous structure is observed throughout the Ta_3N_5/NbN_x film, due to the oxidation of the metallic film and the substitution of O^{2-} ions by N^{3-} ions during the nitridation process, just as occurs during the nitridation of Ta_2O_5 powder to Ta_3N_5. Despite its porous structure, the NbN_x layer is in intimate contact with the

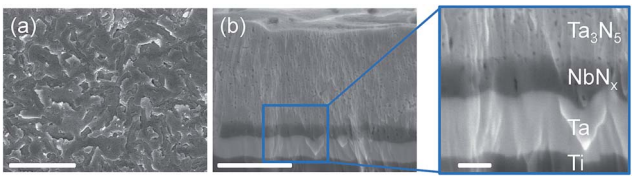

Fig. 2 (a) Top-view and (b) cross-sectional SEM images of a Ta_3N_5/NbN_x/Ta/Ti film. The scale bars are (a) 5 μm, (b) 500 nm, and 100 nm for the zoomed image.

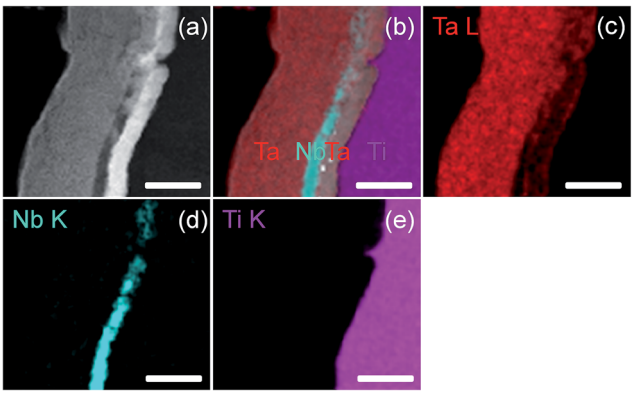

Fig. 3 (a) Cross-sectional STEM image of a Ta_3N_5/NbN_x/Ta/Ti film and (b)–(e) EDX elemental mappings of the image in (a). All scale bars are 500 nm.

Ta_3N_5 film and the Ta contact layer. The EDX mapping images (Fig. 3) demonstrate that the distribution of Nb was confined to the interlayer region, so there was no appreciable doping of Nb into the Ta_3N_5 film.

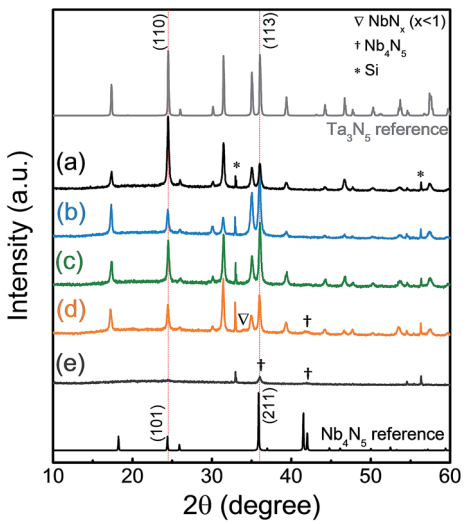

Fig. 4 XRD patterns of (a) Ta_3N_5/Si, (b)–(d) NbN_x/Ta_3N_5/Si with NbN_x thicknesses of (b) 50, (c) 100, and (d) 200 nm, and (e) NbN_x (100 nm)/Si samples. XRD patterns of Nb_4N_5 (PDF# 74-0606) and Ta_3N_5 (PDF# 79-1533) are presented at the bottom and the top, respectively, as references.

Fig. 4 presents the XRD patterns of $NbN_x/Ta_3N_5/Si$ samples with different NbN_x thicknesses prior to the thin film transfer, as a means of confirming the nitridation products. A Ta_3N_5 phase was evidently formed regardless of whether a NbN_x layer was present or not. In addition, impurity phases such as TaN_x or SiN_x were absent. The diffraction pattern of the NbN_x layer deposited on a Si substrate (Fig. 4(e)) suggests that Nb_4N_5 was the main phase formed in the $NbN_x/Ta_3N_5/Si$ sample, although the crystallinity of this specimen was low, and the diffraction peaks of the (101) and (211) planes of the Nb_4N_5 overlap with those generated by the (110) and (113) planes of the Ta_3N_5 at 24.4° and 36.0°, respectively. A peak attributable to NbN_x ($x \leq 1$) was also detected at 34.0° when the thickness of the NbN_x layer was at its maximum (200 nm). Nevertheless, the XRD peaks obtained from the $NbN_x/Ta_3N_5/Si$ primarily provide information regarding the Ta_3N_5 phase because the Ta_3N_5 peaks are much stronger than those generated by the Nb_4N_5 and other NbN_x phases. It should also be noted that Nb_3N_5 was not observed, as expected because Nb^{5+} is prone to reduction to Nb^{4+} or lower-valence nitride species.[27]

The crystallite sizes of the Ta_3N_5 films were calculated from the (110) diffraction peak at 24.4°. The data in Table 1 demonstrate that each of the Ta_3N_5 films had almost identical average crystallite sizes, in the range of 40–45 nm. Thus, the effect of the NbN_x layer on the crystallite size in the Ta_3N_5 film was not significant. Notably, the intensity ratio (R_{in}) obtained from the peaks at 24.4° and 36.0°, which correspond to the (110) and (113) planes of Ta_3N_5, decreased from 2.4 to 0.5–0.8 when NbN_x layers were present on the Ta_3N_5 films.

The crystalline growth of each Ta_3N_5 film was examined in detail by acquiring cross-sectional TEM images of Ta_3N_5/NbN_x films (Fig. 5). These bright field (BF) zone-axis TEM images provide a clear view of the multi-layered structure of the Ta_3N_5/NbN_x/Ta samples, and the bright spots scattered within the darker contrast can provide information regarding the sizes and boundaries of individual grains. In Fig. 5(a) and (b), a high density of bright spots is observed throughout the 100 nm-thick NbN_x interlayer, suggesting that the grain size of the NbN_x phase was much less than the layer thickness of 100 nm (likely below 10 nm). This result agrees with the low-crystalline Nb_4N_5 phase indicated by the XRD patterns in Fig. 4. Notably, the Ta_3N_5 region close to the Ta_3N_5/NbN_x interface generated fewer bright spots when over 200 nm in thickness, as shown in Fig. 5(c), indicating the presence of fewer boundaries among the Ta_3N_5 grains near the interface with the NbN_x layer, while the rest of the Ta_3N_5 film exhibited a number of bright spots.

Selected area electron diffraction (SAED) patterns taken from the regions at 100 nm to the film surface and 100 nm to the Ta_3N_5/NbN_x interface are displayed in the insets of Fig. 5(b) and (c), respectively. The Ta_3N_5 near the interface with the NbN_x generated a more ordered diffraction pattern compared to the Ta_3N_5 close to the surface, which was characterized by random diffractions. This finding indicates that the arrangement of the Ta_3N_5 grains was well oriented in the vicinity of the NbN_x interlayer. It should be noted that crystallite orientation was not observed at the interface between the Ta_3N_5 film and the Ta/Ti substrate of the Ta_3N_5/Ta/Ti film without a NbN_x interlayer, as seen in Fig. S2.†

As suggested by the SAED pattern, the formation of a highly oriented 200 nm Ta_3N_5 layer is not continuous throughout the entirety of the 630 nm Ta_3N_5 film. The growth mode of the Ta_3N_5 film in the presence of the NbN_x interlayer appears to be consistent with that observed for Ta_3N_5 films directly grown on Ta foil substrates by thermal nitridation, as reported by Pinaud *et al.*[18] The electrochemically active surface areas (ECSAs) of the Ta_3N_5 films fabricated by Pinaud's group were found to exhibit minimal change up to a film thickness of 260 nm due to the growth of a compact Ta_3N_5 film. However, the ECSA increased by one or two orders of magnitude when the film thickness was increased from 260 to 630 nm, owing to the growth of disordered layers over top of the compact Ta_3N_5 films. The formation of an oriented Ta_3N_5 layer was also observed in the present Ta_3N_5 films grown on Ta foil substrates (Fig. S3†). Therefore, it is believed that both Ta_3N_5 films grown on Ta substrates and films nitrided in contact with a NbN_x interlayer have similar growth mechanisms, presumably involving Ta_4N_5 and Nb_4N_5 with the same crystal structures[28,29] acting as interlayers, respectively.

Table 1 Average crystallite sizes in Ta_3N_5 films with different NbN_x layer thicknesses, as estimated from XRD peaks at 24.4°, as well as the ratios of the (110) and (113) diffraction intensities of the peaks at 24.4 and 36.0°

NbN_x thickness (nm)	Crystallite size (nm)	Peak intensity ratio
0	42.6 ± 1.8	2.4 ± 0.2
50	44.3 ± 1.8	0.5 ± 0.1
100	41.8 ± 4.4	0.7 ± 0.2
200	42.0 ± 2.7	0.8 ± 0.1

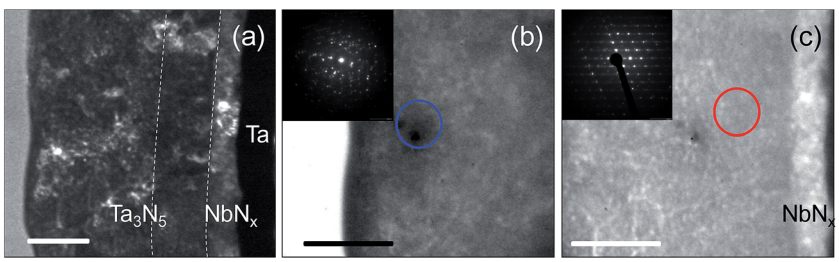

Fig. 5 (a) Zone-axis TEM images of the cross-section of a Ta_3N_5 film on a Ta/Ti substrate with a NbN_x interlayer. The region (200 nm thick) within the white dashed lines represents the oriented Ta_3N_5 layer. SAED patterns of Ta_3N_5 crystallinites near (b) the surface of the Ta_3N_5 film, and (c) the interface of the Ta_3N_5/NbN_x. The insets are diffraction patterns from the selected regions highlighted by the circles. All scale bars are 200 nm.

Photoelectrochemical properties

Current–potential curves obtained from the Ta_3N_5 film photoelectrodes deposited with a layer of $Co(OH)_x$ as an OER catalyst are shown in Fig. 6(a). In the absence of the NbN_x interlayer, the Ta_3N_5 photoelectrode exhibited an anodic photocurrent of approximately 2.0 mA cm^{-2} at 1.23 V *vs.* RHE. The photocurrent densities increased significantly for the Ta_3N_5 films with NbN_x interlayers 50–100 nm in thickness. However, the higher resistance of the NbN_x (Nb_4N_5) interlayer compared to that of the metallic Ta substrate lowered the electron mobility. As a result, the photocurrent decreased as the thickness of the NbN_x interlayer was increased from 100 to 200 nm. Moreover, the onset potential of the photoanodic current generated by the Ta_3N_5/NbN_x (100 nm)/Ta/Ti electrode shifted cathodically by 0.1 V from 0.9 V *vs.* RHE relative to the Ta_3N_5/Ta/Ti electrode. The NbN_x (Nb_4N_5 or NbN) phase acts as a conductive contact for the transport of the majority charge carriers (electrons) collected from the Ta_3N_5 film.

To confirm that the enhancement of the photocurrent of Ta_3N_5/NbN_x photoanodes is associated with the PEC water oxidation performance, gaseous H_2 and O_2 evolved at the counter electrode and the photoanode at 1.0 V *vs.* RHE were analyzed using a micro gas chromatograph (Fig. 6(b)). It was confirmed that the amounts of H_2 and O_2 were virtually equal to the values calculated based on the total charge passed through the system. In addition, the ratio of H_2 to O_2 was close to 2 : 1. These results indicate that the faradaic efficiency during the OER process was unity when employing the Ta_3N_5/NbN_x photoanode. However, the gas evolution rates decreased in accordance with changes in the photocurrent over time, as can be seen in Fig. 6(c). The decreased photocurrent and O_2 evolution rate likely resulted from dissolution of the Co-based catalysts from the surface of the Ta_3N_5 film into the electrolyte solution.[30] The loss of the Co-based catalyst led to direct exposure of the Ta_3N_5 film to the electrolyte solution, and consequently to gradual degradation of the photoanode because bare Ta_3N_5 photoanodes are prone to photocorrosion.[31] A uniform coverage of the Ta_3N_5 electrode with protective and catalytic layers is likely to stabilize the photocurrent. In addition, the Co-based catalyst can be replaced by other oxygen-evolution catalysts (*e.g.* NiO_x), which are electrochemically stable against the dissolution under alkaline conditions.

The IPCE spectra shown in Fig. 7 are consistent with the increases in photocurrent densities brought about by the NbN_x interlayers (see Fig. 6(a)). The onset of a photoresponse at 600 nm corresponds to the direct band gap of Ta_3N_5 at 2.1 eV. It should be noted that a shoulder is observed at 500 nm in each of the IPCE plots. This is also ascribed to the direct transition of Ta_3N_5 between the N 2p and Ta 5d states, as was suggested by earlier optical and theoretical studies of Ta_3N_5 films.[17,32] The IPCEs of Ta_3N_5/NbN_x photoelectrodes at 400–550 nm were evidently increased compared to the bare Ta_3N_5 photoelectrode. Because less than 5% of light can traverse through the Ta_3N_5 film to the NbN_x interlayer below 550 nm (see Fig. S4†), it is unlikely that the photoresponse of the Ta_3N_5/NbN_x electrode was affected by the light absorption characteristics of the NbN_x interlayer and the Ta_3N_5/NbN_x interface. Therefore, it is thought that the enhancements in the IPCE and the photocurrent density of the Ta_3N_5/NbN_x photoelectrodes are primarily due to the changes in the structural features of the Ta_3N_5 film induced by the NbN_x interlayer.

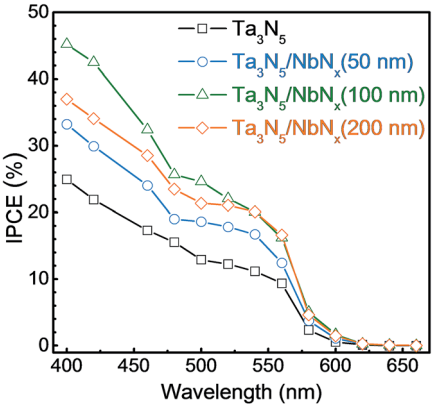

Fig. 7 IPCE spectra of Ta_3N_5/Ta/Ti and Ta_3N_5/NbN_x/Ta/Ti photoelectrodes with different NbN_x interlayer thicknesses.

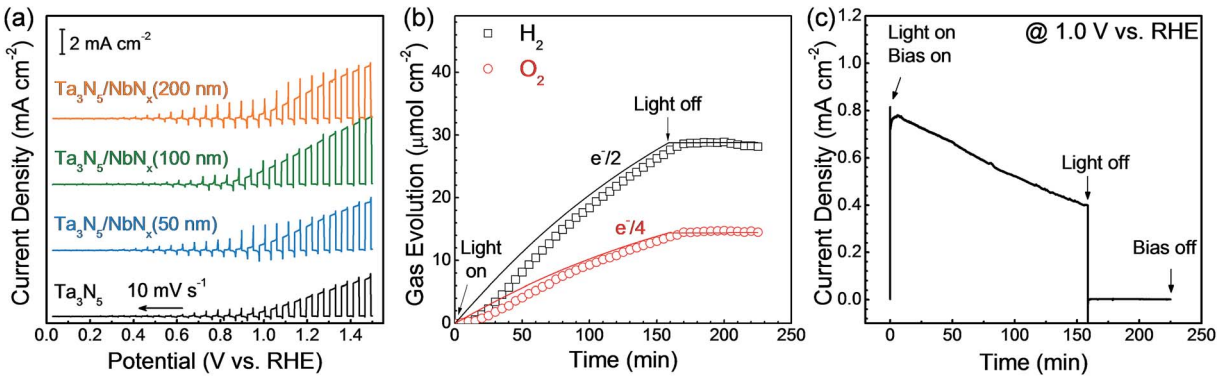

Fig. 6 (a) Current–potential curves obtained from Ta_3N_5/Ta/Ti and Ta_3N_5/NbN_x/Ta/Ti photoelectrodes with different NbN_x interlayer thicknesses, (b) hydrogen and oxygen gas evolution with respect to the total charge passed, as calculated from the (c) current–time curve obtained from the $Co(OH)_x/Ta_3N_5/NbN_x$ (100 nm)/Ta/Ti photoelectrode held at 1.0 V *vs.* RHE. The PEC activities and gas evolution were assessed in a 0.5 M potassium phosphate solution (pH 13) under simulated AM 1.5G light.

Charge separation and transport

In the PEC water oxidation process, light harvesting, charge separation and transport, and hole injection are the three key processes that define the PEC activity and IPCE. The light harvesting of the Ta_3N_5 films would not be expected to have been altered by the NbN_x interlayers because the film thickness and crystallite size were unchanged. It is also believed that the hole injection process was not affected by the presence of the interlayer because of the similarities in the roughness factors, flat band potentials, and donor densities. ECSA values were estimated from the double-layer charging in the cyclic voltammograms (CVs) as a means of examining the surface roughness of the Ta_3N_5 electrodes (Fig. S5†), and the roughness factor was found to be barely changed by the presence of the NbN_x interlayer. Mott–Schottky plots (Fig. S6†) were used to estimate the flat band potentials and the carrier densities, with values of −0.06 and −0.08 V *vs.* RHE, respectively. Hence, charge separation and transport are evidently the major factors contributing to the enhancement of the photocurrent by the NbN_x interlayer. Electrochemical impedance spectra (EIS) of Ta_3N_5 and Ta_3N_5/NbN_x electrodes are shown in Fig. 8. The Nyquist plots with a feature of single capacitance were fitted using the Randles equivalent circuit model, similar to the case for hematite photoanodes in the presence of $[Fe(CN)_6]^{3-/4-}$ redox couples.[33] This equivalent circuit consists of the series resistance (R_s) of the NbN_x and Ta/Ti layers, the capacitance of the bulk Ta_3N_5 film (CPE), and the charge transfer resistance from the valence band of Ta_3N_5 to the solution (R_{CT}), which may be associated with resistances representing bulk recombination and charge transfer at the electrolyte/semiconductor interface. The values of the charge transfer resistance (R_{CT}, Table S1†) of all the Ta_3N_5/NbN_x photoelectrodes were smaller than that of the unmodified Ta_3N_5 photoelectrode although the surface reaction was the same, oxidation of sulfite ions on the Ta_3N_5 surface. This result suggests an increase in the population of holes that survive recombination with electrons and successfully reach the semiconductor/liquid junction as a result of promotion of charge separation and transport process by the NbN_x interlayers. The R_s increased with the thickness of the NbN_x layer because of its lower conductivity. However, the contribution of R_s to the total resistance is negligible.

Two charge generation and transport scenarios can be considered, depending on whether photons are absorbed near the Ta_3N_5 film surface (case i) or the Ta_3N_5/NbN_x interface (case ii), as depicted in Fig. 9. Long-distance electron transport and short-distance hole transport occur in the former case (i) while long-distance hole transport and short-distance electron transport take place in the latter case (ii). The analysis of the integrated photocurrent calculated on the basis of the standard AM 1.5G (ASTM G173-03) spectrum and the IPCE spectra (Fig. S7†) indicates that the short-wavelength light absorbed near the Ta_3N_5/NbN_x electrode surface showed a larger contribution to the enhancement in photocurrent than the long-wavelength light absorbed near the Ta_3N_5/NbN_x interface. The formation of an oriented Ta_3N_5 layer (200 nm thick) by the NbN_x interlayer probably promotes the electron mobility in the Ta_3N_5 film near the Ta_3N_5/NbN_x interface. Therefore, photogenerated charges near the surface may contribute to the PEC water oxidation more effectively in the presence of a NbN_x interlayer, given that the migration distance required for holes to reach the surface is shorter in a disordered Ta_3N_5 layer. Nevertheless, it should be pointed out that the photons absorbed near the Ta_3N_5/NbN_x interface are not necessarily utilized efficiently even in the presence of a NbN_x interlayer because holes generated deeper in the Ta_3N_5 film have a higher probability of recombining with electrons before reaching the surface, since the hole mobility is lower than the electron mobility.[17] As a consequence, the photocurrent observed in the present study was still lower than the maximum theoretical value for Ta_3N_5, so it is most likely necessary to tune the thicknesses of the oriented and disordered Ta_3N_5 layers.

A photoanode configuration consisting of a lower oriented Ta_3N_5 layer and an upper disordered Ta_3N_5 layer represents a combination of a short migration distance for photoexcited holes and efficient electron transport toward the back conductor layer. The introduction of the NbN_x interlayer effectively realizes this ideal photoanode configuration and thus enhances the PEC performance. This result suggests that the structural and PEC properties of Ta_3N_5 photoanodes can be improved by designing appropriate interlayers, regardless of the nitridation of the Ta_3N_5 film and the particular back conductor material employed. The

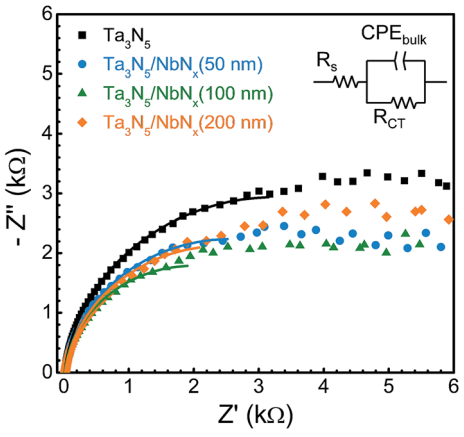

Fig. 8 Nyquist plots of electrochemical impedance spectra of Ta_3N_5 and Ta_3N_5/NbN_x electrodes measured under simulated AM 1.5G light in a 0.5 M KPi solution (pH 13) with a sacrificial reagent (0.5 M SO_3^{2-}) at 1.0 V *vs.* RHE. The inset represents the Randles equivalent circuit used for fitting the Nyquist plots.

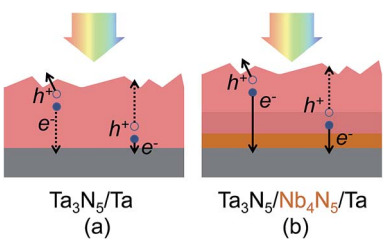

Fig. 9 Schematic depicting the separation and transport of photogenerated electrons and holes in (a) Ta_3N_5/Ta and (b) Ta_3N_5/NbN_x/Ta films.

film transfer method developed in this study presents a means of studying such aspects owing to the controllability of the thickness and the stacking order of multilayers.

Conclusions

NbN_x layers principally consisting of Nb_4N_5 were introduced as interlayers between Ta_3N_5 films and the back substrate, using the film transfer method. The Nb_4N_5 interlayer did not change the phase purities and the crystallite sizes of the Ta_3N_5 films significantly, although the preference in the crystalline orientation of the Ta_3N_5 film was enhanced by the Nb_4N_5 phase. The photocurrents obtained from Ta_3N_5 photoanodes during the PEC water oxidation reaction increased significantly in the presence of the NbN_x interlayer. The results of zone-axis imaging and electron diffraction from cross-sectional TEM revealed that ordered growth of the Ta_3N_5 film occurred and that a 200 nm layer of highly grain-oriented Ta_3N_5 was formed near the Ta_3N_5/NbN_x interface. The formation of an oriented Ta_3N_5 layer did not affect the ECSA, flat band potential or carrier density of a 630 nm Ta_3N_5 film. The increased photocurrent associated with the presence of a NbN_x interlayer is primarily attributed to the increased long distance electron mobility in the Ta_3N_5 film. The film growth on the Nb_4N_5 layer observed in this work demonstrates the key roles of a buffer layer in the design and synthesis of efficient Ta_3N_5 photoelectrodes.

Acknowledgements

This work was financially supported by Grants-in-Aid for Specially Promoted Research (No. 23000009) and for Young Scientists (A) (No. 15H05494) and Young Scientists (B) (No. 5K17895) of Japan Society for the Promotion of Science (JSPS). This work was partly supported by the Artificial Photosynthesis Project of the New Energy and Industrial Technology Development Organization (NEDO) and Companhia Brasileira de Metalurgia e Mineração (CBMM). Part of this work was conducted at the Research Hub for Advanced Nano Characterization at the University of Tokyo, under the support of the "Nanotechnology Platform" (project No. 12024046) of the Ministry of Education, Culture, Sports, Science and Technology (MEXT), Japan. The authors thank Dr Qian Wang, Dr Miao Zhong, Dr Taro Yamada and Mr Yutaka Sasaki of the University of Tokyo for SEM characterisation and discussion.

References

1 A. J. Nozik, *Annu. Rev. Phys. Chem.*, 1978, **29**, 189–222.
2 M. Grätzel, *Nature*, 2001, **414**, 338–344.
3 A. Fujishima and K. Honda, *Nature*, 1972, **238**, 37–38.
4 W. J. Chun, A. Ishikawa, H. Fujisawa, T. Takata, J. N. Kondo, M. Hara, M. Kawai, Y. Matsumoto and K. Domen, *J. Phys. Chem. B*, 2003, **107**, 1798–1803.
5 T. W. Kim and K.-S. Choi, *Science*, 2014, **343**, 990–994.
6 Y. Li, T. Takata, D. Cha, K. Takanabe, T. Minegishi, J. Kubota and K. Domen, *Adv. Mater.*, 2013, **25**, 125–131.
7 M. Zhong, Y. Ma, P. Oleynikov, K. Domen and J.-J. Delaunay, *Energy Environ. Sci.*, 2014, **7**, 1693–1699.
8 H. X. Dang, N. T. Hahn, H. S. Park, A. J. Bard and C. B. Mullins, *J. Phys. Chem. C*, 2012, **116**, 19225–19232.
9 T. Minegishi, N. Nishimura, J. Kubota and K. Domen, *Chem. Sci.*, 2013, **4**, 1120–1124.
10 K. Ueda, T. Minegishi, J. Clune, M. Nakabayashi, T. Hisatomi, H. Nishiyama, M. Katayama, N. Shibata, J. Kubota, T. Yamada and K. Domen, *J. Am. Chem. Soc.*, 2015, **137**, 2227–2230.
11 Y. Li, L. Zhang, A. Torres-Pardo, J. M. Gonzalez-Calbet, Y. Ma, P. Oleynikov, O. Terasaki, S. Asahina, M. Shima, D. Cha, L. Zhao, K. Takanabe, J. Kubota and K. Domen, *Nat. Commun.*, 2013, **4**, 2566.
12 S. Hu, M. R. Shaner, J. A. Beardslee, M. Lichterman, B. S. Brunschwig and N. S. Lewis, *Science*, 2014, **344**, 1005–1009.
13 L. Chen, J. Yang, S. Klaus, L. J. Lee, R. Woods-Robinson, J. Ma, Y. Lum, J. K. Cooper, F. M. Toma, L. W. Wang, I. D. Sharp, A. T. Bell and J. W. Ager, *J. Am. Chem. Soc.*, 2015, **137**, 9595–9603.
14 G. Liu, J. Shi, F. Zhang, Z. Chen, J. Han, C. Ding, S. Chen, Z. Wang, H. Han and C. Li, *Angew. Chem., Int. Ed.*, 2014, **53**, 7295–7299.
15 G. Liu, P. Fu, L. Zhou, P. Yan, C. Ding, J. Shi and C. Li, *Chem.–Eur. J.*, 2015, **21**, 9624–9628.
16 J. Seo, T. Takata, M. Nakabayashi, T. Hisatomi, N. Shibata, T. Minegishi and K. Domen, *J. Am. Chem. Soc.*, 2015, **137**, 12780–12783.
17 J. M. Morbec, I. Narkeviciute, T. F. Jaramillo and G. Galli, *Phys. Rev. B*, 2014, **90**, 155204.
18 B. A. Pinaud, P. C. K. Vesborg and T. F. Jaramillo, *J. Phys. Chem. C*, 2012, **116**, 15918–15924.
19 M. X. Li, W. J. Luo, D. P. Cao, X. Zhao, Z. S. Li, T. Yu and Z. G. Zou, *Angew. Chem., Int. Ed.*, 2013, **52**, 11016–11020.
20 B. A. Pinaud, A. Vailionis and T. F. Jaramillo, *Chem. Mater.*, 2014, **26**, 1576–1582.
21 S. Nakamura, *Jpn. J. Appl. Phys.*, 1991, **30**, 1705–1707.
22 F. A. Ponce and D. P. Bour, *Nature*, 1997, **386**, 351–359.
23 A. Dabirian and R. van de Krol, *Chem. Mater.*, 2015, **27**, 708–715.
24 G. Liu, S. Ye, P. Yan, F. Xiong, P. Fu, Z. Wang, Z. Chen, J. Shi and C. Li, *Energy Environ. Sci.*, 2016, **9**, 1327–1334.
25 C. Wang, T. Hisatomi, T. Minegishi, M. Nakabayashi, N. Shibata, M. Katayama and K. Domen, *Chem. Sci.*, 2016, **7**, 5821–5826.
26 C. C. L. McCrory, S. Jung, J. C. Peters and T. F. Jaramillo, *J. Am. Chem. Soc.*, 2013, **135**, 16977–16987.
27 R. Fix, R. G. Gordon and D. M. Hoffman, *Chem. Mater.*, 1993, **5**, 614–619.
28 T. Nobuzo, *Jpn. J. Appl. Phys.*, 1971, **10**, 248–259.
29 G. Oya and Y. Onodera, *J. Appl. Phys.*, 1974, **45**, 1389–1397.
30 G. M. Carroll, D. K. Zhong and D. R. Gamelin, *Energy Environ. Sci.*, 2015, **8**, 577–584.
31 S. Chen and L.-W. Wang, *Chem. Mater.*, 2012, **24**, 3659–3666.
32 A. H. Reshak, *Comput. Mater. Sci.*, 2014, **89**, 45–51.
33 B. Klahr, S. Gimenez, F. Fabregat-Santiago, J. Bisquert and T. W. Hamann, *Energy Environ. Sci.*, 2012, **5**, 7626–7636.